Composition-dependent chemical ordering predicted in Pt–Ag nanoalloys

Alexis Front, Christine Mottet

Composition-dependent chemical ordering predicted in Pt-Ag nanoalloys

Alexis Front[a,b] and Christine Mottet[a]

Pt-Ag nanoalloys display an astonishing chemical organization depending on size and composition. It has been shown recently a reversed size-dependent stabilization of ordered nanophases [Pirart *et al., Nature Communications*, 2019, 10, 1982] around equiconcentration. We extend this study by a theoretical investigation on the whole range of composition showing a significant composition-dependent chemical ordering in Pt-Ag nanoalloys. At low silver content, the surface exhibits a strong Ag segregation coupled to a (2x1) superstructure on the (100) facets. By increasing silver concentration, the system displays an $L1_1$ ordered phase in the core, interrupted in a narrow range of concentration by a concentric multishell structure characterized by an alternation of Ag-pure/Pt-pure concentric layers starting from the surface shell to the core. Experimentally, the $L1_1$ ordered phase has been observed whereas the concentric multishell structure is lacking due to the difficulty of the experimental characterization.

1 Introduction

Nanoalloys is a term to designate nanoparticles of metallic alloys where both size and composition induce attractive properties in catalysis, optics or magnetism.[1–4] For example in electrocatalysis, Pt-based nanocatalyst are vastly investigated in order to keep the high catalytic activity of platinum while in the same time reducing platinum content and therefore the global cost.[5] Intermetallic Ag-Pt surfaces are highly active for electrochemical oxidation of formic acid[6,7] or in selective methanol oxidation to methyl formate.[8] Under the shape of nanoparticles, Ag-Pt stellated bimetallic nanoparticles[9], core-shell nanoparticles[10] or nanocages[11] demonstrated enhanced electrochemical activity for methanol oxidation and oxygen reduction reactions. Concerning the direct synthesis of H_2O_2 from dihydrogen and dioxygen, Ag-Pt octahedra have shown to increase by a factor ten the selectivity compared to pure Pt octahedra.[12,13] A crucial point to be used as electrocatalysts in a PEM fuel cell is their stability and durability in reaction conditions.[11,14,15] An other interesting aspect of Pt-Ag nanoboxes synthesized by galvanic replacement reactions are their optical properties and the possibility to tune the surface plasmon resonnance peak across the entire visible spectrum.[16] To better understand the relation between structure and properties we present here a theoretical study of the structure and chemical ordering of Pt-Ag nanoalloys as it has been done with other systems (Ag-Cu, Ag-Co, Ag-Ni, and Au-Ni nanoalloys).[17] The originality of Pt-Ag system resides in its hybrid chemical tendency. According to the bulk phase diagram[18–20], Pt-Ag system displays a wide immiscible domain as in the case of Ag-Cu, Ag-Co or Ag-Ni systems but, in addition, it presents an intermetallic compound around equiconcentration with the $L1_1$ ordered structure. In general, face centered cubic metallic alloys at equiconcentration display the $L1_0$ ordered phase with an alternation of pure atomic plans in the (100) direction, as in the well known Cu-Au or Co-Pt systems.[21,22] In the case of Ag-Pt, the $L1_1$ ordered phase forms an alternation of pure atomic plans in the (111) direction, as for Cu-Pt alloys, the only known one.[23] To characterize the Pt-Ag nanoalloys, we have determined a realistic interatomic potential for the Pt-Ag system[24,25] able to reproduce the main chemical tendencies of the bulk phase diagram. As mentioned before, this system presents an immiscible gap rather extended in the Pt-rich side, and the $L1_1$ ordered phase at equiconcentration. This leads, in bulk alloys for intermediate compositions, to a phase coexistence between this ordered intermetallic phase and an almost Pt-pure or Ag-pure phase. At the nanoscale, the phase separation tendency is a driving force to surface segregation, and, in the same time, the $L1_1$ ordered phase could coexist depending on the concentration and the temperature. This raises

[a] *Aix-Marseille University / CNRS, CINaM UMR 7325, Campus de Luminy, 13288 Marseille, France. E-mail: christine.mottet@univ-amu.fr*

[b] *Present address:Department of Chemistry and Materials Science, Aalto University, 02150 Espoo, Finland; Department of Applied Physics, Aalto University, FI-00076 Espoo, Finland.*

to the main interrogation of this study: which chemical configurations are stabilized in nanoalloys ? A theoretical study at high temperature near the melting transition has been performed with the same interatomic potential on Pt-Ag nanoalloys for the three intermediate compositions $AgPt_3$, AgPt and Ag_3Pt showing the influence of Ag surface segregation on premelting.[26] Concerning the core, optical properties and chemical ordering of Pt-Ag nanoalloys have been addressed[27] and compared to other similar systems mixing coinage metals (Ag, Au) with (Pt, Pt) transition metals.[28] It has been shown that the remarkable $L1_1$ ordering was only favoured in small AgPt particles but the chemical ordering in the core does not induce specific optical signature.

2 Theoretical model and numerical simulations

The energetic model to represent the interactions between the atoms is a many-body potential based on a tight-binding framework within the second moment approximation (TB-SMA) of the density of states of d-band, well fitted for transition and noble metals.[29] The originality of this potential, in the case of Pt-Ag system, is to reproduce bulk phase diagram properties, notably the quite rare ordered $L1_1$ phase at equiconcentration formed by an alternation of pure (111) atomic layers[18–20] as in the better known Cu-Pt system.[23,30] The TB-SMA interatomic potential has been modified to stabilize the specific $L1_1$ phase at equiconcentration by adding an attractive contribution with a gaussian shape. This Gaussian function is localized at the second neighbour distance where the mixed bonds are responsible of the stabilization of the $L1_1$ phase as compared to the $L1_0$ one. This original potential is written as follows with an attractive term (bonding origin) including a classical square root dependence with the neighboring atoms and a gaussian contribution centered on the second neighbors distance:

$$E_i^{Bond} = -\sqrt{\sum_{j,r_{ij}<r^3_{\alpha\beta}} \xi^2_{\alpha\beta} e^{-2q_{\alpha\beta}\left(\frac{r_{ij}}{r^0_{\alpha\beta}}-1\right)}} - \sum_{j,r_{ij}<r^3_{\alpha\beta}} G_{\alpha\beta} e^{-\frac{(r_{ij}-r_2)^2}{2\sigma^2_{\alpha\beta}}} \quad (1)$$

and an empirically repulsive term of the Born-Mayer type:

$$E_i^{Rep} = \sum_{j,r_{ij}<r^3_{\alpha\beta}} A_{\alpha\beta} e^{-p_{\alpha\beta}\left(\frac{r_{ij}}{r^0_{\alpha\beta}}-1\right)} \quad (2)$$

where (α,β) is the nature of the metal atom. In these expressions, r_{ij} is the distance between the atom at site i and their neighbors at site j, $r^3_{\alpha\beta}$ is a cutoff distance for the third neighbor distance and $r^0_{\alpha\beta}$ is the first neighbor distance depending on the nature of the atoms.

Table 1 TB-SMA interatomic potential parameters. $r^3_{\alpha\beta}$ represents a cut-off distance around the 3rd neighbors where the effective TB-SMA potential is connected to a polynomial form of the potential between third and fourth neighbors distance and $r^4_{\alpha\beta}$ represents the cutoff distance around the 4th neighbors where the potential is zero.

$\alpha-\beta$	$p_{\alpha\beta}$	$q_{\alpha\beta}$	$A_{\alpha\beta}$	$\xi_{\alpha\beta}$	$r^3_{\alpha\beta}$	$r^4_{\alpha\beta}$
Pt-Pt	10.7960	3.1976	0.1993	2.2318	4.8745	5.6286
Ag-Ag	11.7240	2.8040	0.0748	1.0064	5.0949	5.8831
Pt-Ag	11.2600	3.0008	0.1456	1.5920	5.0949	5.6286

The homo-atomic ($\alpha=\beta$) parameters are fitted to the cohesive energies, lattice parameters and elastic constants calculated by density functional theory (DFT). For the hetero-atomic interactions ($\alpha\neq\beta$), the parameters $p_{\alpha\beta}$ and $q_{\alpha\beta}$ are the average of the pure metal ones. Finally, $A_{\alpha\beta}$, $\xi_{\alpha\beta}$, $G_{\alpha\beta}$ and $\sigma_{\alpha\beta}$ are fitted to the formation enthalpies of the $L1_0$ and the $L1_1$ phases as well as the solution energies of one impurity in the matrix of the other metal. $G_{\alpha\beta}$=0.0440 eV and $\sigma_{\alpha\beta}$=0.1393 Angströms. More details on the fitting procedure can be found in Ref.[25].

Monte Carlo simulations are performed in the semi-grand canonical ensemble using the Metropolis algorithm[31] which means that the total number of atoms in the binary system, the temperature and the pressure are fixed whereas the number of atoms per species can change. As a consequence, the concentration at equilibrium is a result of the Monte Carlo process. In the Metropolis algorithm, starting with the system in the "i" state, with energy $E(i)$, one performs one atomic trial, which can be either moving an atom or permuting the chemical nature of an atom, we calculate the new energy $E(j)$. If $E(j)$ is lower than $E(i)$, the new configuration is accepted and the simulation goes on starting from it, else, the "j" state is accepted according to the following probability:

$$\exp\left[-\frac{E(j)-E(i)+dn(\mu_B-\mu_A)+\frac{3}{2}\ln(\frac{m_B}{m_A})}{k_BT}\right] \quad (3)$$

where dn is the permutation sign equal to 1 if we permute an atom of type A into an atom of type B or -1 if we permute an atom of type B into an atom of type A. m_A and m_B are the atomic mass of the elements A and B.

In a standard Monte Carlo simulation with N atoms we run five to ten thousands macrosteps after leaving the system being equilibrated during two to five thousands steps. One macrostep consists in proposing randomly either displacements of atoms or permutations of chemical species, N-times. We usually start with a Pt-pure or Ag-pure system and increase, respectively decrease the chemical potential difference $\mu_B-\mu_A$ in order to scan the entire concentra-

tion range and we start the new Monte Carlo run for each chemical potential from the last configuration.

Finally we calculated the atomic local stress on each atomic site of the nanoalloys after optimizing the atomic structure at 0 K. The local atomic pressure formula is given by Kelires and Tersoff[32]:

$$p_i = -\frac{dE_i}{dlnV_i} \tag{4}$$

where E_i is the energy on site i and V_i the atomic volume proportional to r_{ij}^3, j designating the neighbor sites of i. This leads to the following expression of the local atomic pressure on site i, expressed in GPa, when the energy E_i is in eV/at.:[33–35]

$$p_i = -400\frac{q_e}{(a_\alpha)^3}\sum_{j,r_{ij}<r_{\alpha\beta}^3}\frac{dE_i}{3dr_{ij}}r_{ij} \tag{5}$$

where a_α is the lattice parameter of the metal of type α (Pt or Ag), in Angströms, and $q_e = 1.60219\ 10^{-19}$ C is the electron charge to convert the eV/at. in GPa, knowing that the atomic volume in the face centered cubic structure is equal to the cube of dimension a_α divided by 4 since there is four atoms per mesh.

The local atomic pressure represents the trace of the stress tensor $\bar{\sigma}$:

$$p_i = -\frac{1}{3}tr(\bar{\sigma}) = -\frac{1}{3}\sum_{i=1,3}\sigma_{ii} \tag{6}$$

It is well to recall that in elasticity the stress is positive for positive strain (extension) and negative for negative strain (contraction) whereas it is the opposite for a pressure since by convention a positive pressure is associated to a compression (i.e. contraction) whereas a negative pressure is associated with a tension (i.e. extension).

3 Results and discussion

We considered truncated octahedra (TOh) of 1289 and 2951 atoms which represent Wulff equilibrium shape on the fcc structure (the one of the bulk Ag and Pt metals) and because experiments have shown essentially fcc structures with that shape for PtAg nanoparticles.[24] We performed semi-grand canonical Monte Carlo simulations to determine isotherms by sweeping the whole range of composition of the alloy. The Monte Carlo simulations give an equilibrium chemical configuration including atomic relaxations for any compositions, at a given temperature, leading to what we call "isotherms" (Fig.1). Thus we characterized the equilibrium chemical configuration of the Pt-Ag nanoalloy by distinguishing the silver concentration on different group of sites of the surface and in the core. Typically we distinguish vertex, edge, (100) and (111) facet sites on the surface (Fig.1-top graph). In the core, we distinguish the concentric shells starting from the surface up to the center of the nanoparticle (Fig.1-middle graph) and the core sublattices (Fig.1-bottom graph), specially determined to characterize the $L1_1$ ordered phase. In fact we chose two sublattices in a (111) atomic plane and the other two in the next (111) plane, in a way to characterize the fcc atomic mesh but in order to distinguish the $L1_1$ phase. These two core site analysis are complementary to give a precise characterization of the chemical ordering in the core of the Pt-Ag TOh. All these specific concentrations are plotted as a function of the global silver concentration of the nanoparticle. These equilibrium concentrations, on well chosen characteristic sites of the nanoalloys, allow to give a precise idea of the chemical configuration of the nanoparticle at any global composition of Pt and Ag. Some of them are illustrated on Fig.2.

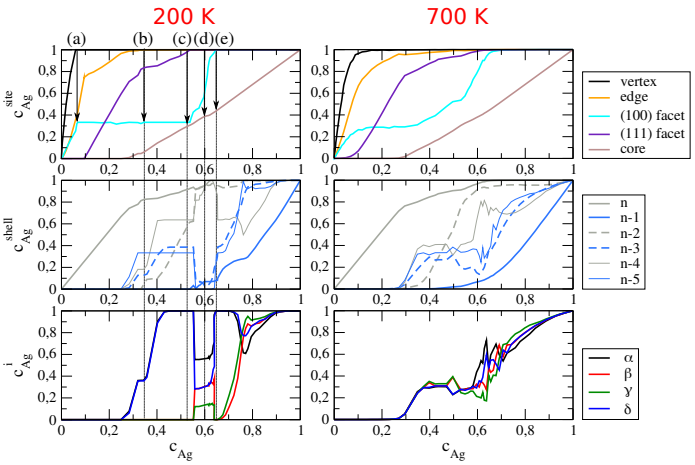

Fig. 1 Isotherms at 200 K and 700 K of the Pt-Ag truncated octahedra of 1289 atoms (around 3 nm): surface site concentration (top), concentric shells concentration (middle), core sublattices concentration (bottom) as a function of the global Ag concentration of the nanoparticle. The concentric shells start from the surface (n) to the center of the nanoparticle (n-5). The core sublattices are considered in the central part of the nanoparticle by removing the three external layers (n, n-1, n-2). The structure corresponding to the compositions indicated by (a-e) are presented in Fig.2.

At low Ag composition, silver atoms occupy first the verteces, followed by the edges and (100) sites simultaneously. The silver edge concentration in Fig.1 concerns two different kind of edges: the one between two (111) facets and the one between (100) and (111) facets. They are occupied differently. At low Ag concentration, only the one between (100) and (111) facets are occupied by silver, as shown in Fig.2-(a). This is correlated to the occupation of the (100) facets. The (100) facets are characterized by an alternation of Ag-pure and Pt-pure atomic rows corresponding to the (2x1) surface reconstruction. This superstructure displays a plateau over a large range of composition (from 7 to 55% of Ag). In the meantime,

the edges between two adjacent (111) facets remain Pt-pure (Fig.2-(a)). It is worth noticing that for this cluster size, the square (100) facets are made of an odd number of atomic rows which allows to form the (2x1) surface reconstruction and to fill the edges with Ag on the border of the facets. In case of an even number of atomic row on the facet, it would lead to a frustration between the (2x1) surface reconstruction and the filling of the edges. The origin of this peculiar chemical ordering on (100) facets comes both from the chemical ordering tendency linked to the $L1_1$ ordered phase and also from the misfit between the two elements bringing elastic strains. However such surface reconstruction depends on temperature and disappears at higher temperature as shown in Fig.1 at 700 K where the plateau is attenuated.

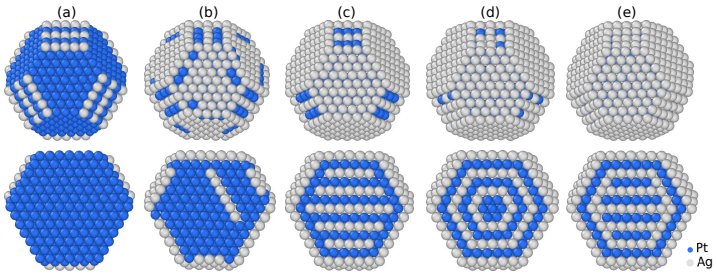

Fig. 2 Snapshots of the TOh_{1289} at 200 K corresponding to the compositions pointed in Fig.1: (a) 7% of Ag, (b) 34% of Ag, (c) 54% of Ag, (d) 61% of Ag and (e) 65% of Ag. The top row represents the external surface whereas the bottom row displays a cutting view. Ag atoms are in grey ant Pt atoms in blue

At 10 % of Ag, the edges curve exhibits an inflexion which concerns the edges between two (111) facets and which is correlated to the filling of the (111) facets by silver. Meanwhile (111) facets begin to be occupied by silver atoms. The Ag concentration on (111) facets is strictly linear up to 70 % corresponding to a Langmuir mode with random occupation sites, weakly temperature-dependent (see Fig.1). We notice an inversion of the usual hierarchy of segregation from the lower coordinated sites to the higher coordinated sites, i.e. between the (100) and (111) facets, because the (111) facets are Ag-pure before the (100) ones. This effect persists at 700 K. This has to be compared with the surprising anisotropy of surface segregation in CuPt alloys surfaces[36] where the Cu surface enrichment is stronger on the close-packed (111) surface than for the more open (100) one.

At 34 % of Ag, (111) facets display a dimming of the Ag enrichment characterized by an inflexion of the curve. This phenomenon is correlated to the filling of the remaining Pt sites located at the outline of the (111) facets, i.e. in contact with the Ag edges (Fig.2-(b)). The (2x1) superstructure on the (100) facets remains up to 55 % of Ag (Fig.1-top graph) whereas all other surface sites are fully occupied by silver atoms.

All these particular chemical configurations on the surface shell of the nanoparticles may have an high impact on catalytic properties with different surface sites occupied either by Ag or by Pt atoms and surrounded respectively by Pt or Ag atoms.

Chemical ordering in the core is characterized by shell concentration (Fig.1-middle graph) and core sublattice occupations (Fig.1-bottom graph). At 34 % of Ag, the core displays alternation of some Ag-pure/Pt-pure (111) atomic planes corresponding to the beginning of the formation of a $L1_1$ ordered phase. By increasing the silver concentration, all the core is ordered according to the $L1_1$ phase up to 54 % of Ag (Fig.2-(c)). On the bottom graph of the Fig.1, the $L1_1$ phase is characterized by two sublattices occupied by Pt (α and δ) and two occupied by Ag (β and γ).

Then, for a concentration slightly higher, around 60 % of Ag (Fig.2-(d)), the nanoparticle is composed of an almost Ag-pure shell (only a few Pt atoms isolated on (100) facets remain) and a core displaying an alternation of Ag and Pt concentric layers. This multishell structure is characterized by an alternation of Ag-rich (grey) and Pt-rich (blue) concentric layers starting from a silver surface (n), then a Pt subsurface (n-1) and so on, as illustrated in the Fig.1 (middle graph). Increasing the Ag composition to 65 %, one recovers the $L1_1$ phase in the core (Fig.2-(e)) but with an alternation over three concentric shells at the vicinity of the surface, remaining from the last structure. To go deeper in the analysis, a decomposition of the core into concentric shells is illustrated in Fig.3. It is worth noticing that the (100) facets of the shell under the surface (namely the n-1 shell) are filled by silver atoms whereas all the other sites are Pt-pure. On the following shell, namely the n-2 shell, (100) facets, which consist in only one atom, are filled by platinum, whereas this shell is Ag-pure. The other shells do not present (100) facets, they are octahedral. The origine of such chemical arrangement may be linked to the peculiar (100) facet reconstruction with a mixed Ag-Pt concentration to accommodate elastic strain. This leads to have pure concentric shells except on the (100) facets of each shell.

Comparing to a higher temperature (700 K), the $L1_1$ ordered phase in the core does no more exist as displayed by the core sublattices occupation on Fig.1 which are almost equaly filled. In the same time, the 3-concentric shells at the vicinity of the surface remain because this phenomenon is driven by surface segregation, whereas the ordered phase is only stabilized beneath a critical order/disorder temperature as in bulk alloys.

The main result which consists in a core, either ordered

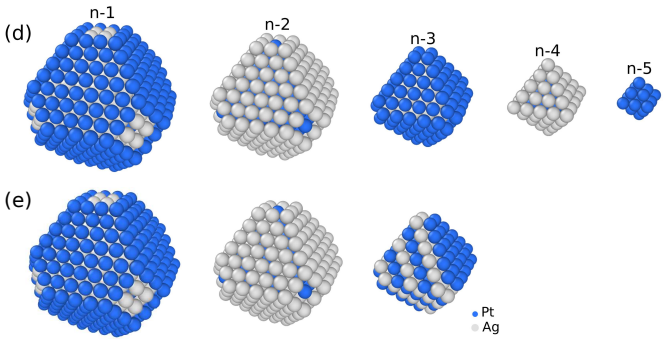

Fig. 3 Decomposition in concentric shells of TOh_{1289} at 200 K corresponding to the compositions (d) multishell structure and (e) $L1_1$ phase surrounded by 3-concentric shells, pointed in Fig.1 and illustrated in Fig.2. Ag atoms are in grey ant Pt atoms in blue.

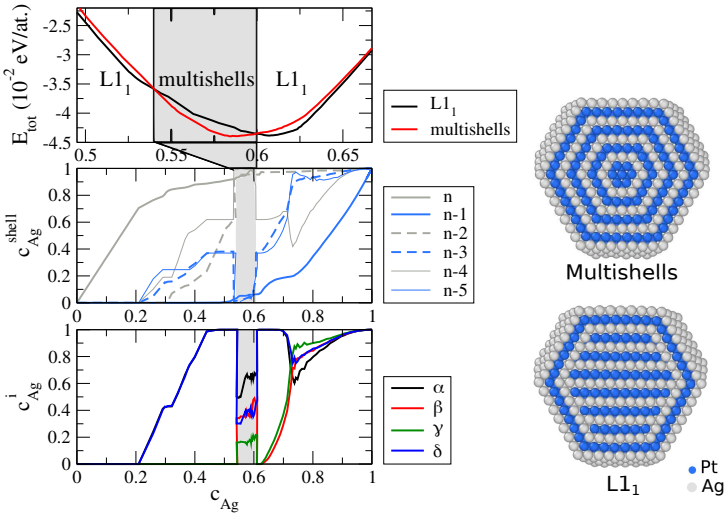

Fig. 4 Isotherms at 300 K of the Pt-Ag truncated octahedra of 2951 atoms (around 5 nm): total energies of the concentric multishells phase and the $L1_1$ phase surrounded by 3-concentric shells (top), concentric shells concentration (middle), core sublattices concentration (bottom) as a function of global Ag concentration. The concentric shells start from the surface (n) to the center of the nanoparticle (n-5). Core sublattices are considered in the central part of the nanoparticle by removing the three external layers (n, n-1, n-2), as in Fig.1. The right column shows cutting view of the two structures. Ag atoms are in grey and Pt atoms in blue.

according to the $L1_1$ phase, or with a concentric multishells structure, depending on the concentration, is general and appears at larger sizes. As an illustration, we have extended the previous investigation to a truncated octahedron of 2951 atoms (around 5 nm). We first compare the energies of the $L1_1$ phase and the multishell structures because the Monte Carlo simulations for large sizes is not able to switch from one structure to the other in the same simulation. In fact, we start with an initial configuration, either the perfect $L1_1$ ordered cluster or the perfect alternation of Pt/Ag concentric shells. For each configuration, we both increase or decrease the chemical potential to cover the entire concentration range. Finally, we keep the curve that minimizes the energy as shown in Fig.4. From 54 % to 60 % of Ag, the concentric multishells structure is stable. Above and below these thresholds, the $L1_1$ phase with a 3-concentric shells is stable. Above 70 % of Ag, all the core sublattices gather corresponding to a solid solution in the Ag-rich side, as in the bulk phase diagram.

This is the first time that such a chemical configuration transition has been predicted on nanoalloys. The concentric multishells structure itself is unusual in binary nanoalloys and has only been observed on fivefold symmetry and $L1_0$ ordered domains in decahedral Co-Pt nanoparticules.[37] The $L1_1$ chemical ordered phase has been experimentally observed recently by high resolution scanning transmission electron microcopy with high angle annular dark field mode (STEM-HAADF).[24] If the experimental studies concluded in the $L1_1$ ordered phase on small nanoparticles (up to 2.5 nm) with a silver surface-shell, it can not fully exclude Pt subsurface segregation. Theoretical investigation showed that Ag surface segregation induces a very strong stress in compression inside the nanoparticle that can be released by putting smaller atoms i.e. Pt atoms on subsurface.[24]

In the present study, we show that the alternation of pure atomic concentric layers which can be seen as an $L1_1$ nanophase on each (111) orientation of the truncated octahedron is in competition with the perfect $L1_1$ phase in the core. By increasing the Ag composition, one of the (111) orientation in the cluster is chosen to display only one $L1_1$ nanophase in the core. It is important to notice that when only one $L1_1$ nanophase exists in the nanoparticle, it can be characterized by STEM-HAADF but the alternated concentric layers not. This can explain why the authors did not observe experimentally this phase. Moreover, the formation of the $L1_1$ induces a rhombohedral deformation along the (111) orientation, as in the CuPt system,[23] which enters in competition with the silver surface segregation. To release the stress, the system forms an alternation of concentric layers near the surface which accommodates the elastic deformation induced by the $L1_1$ phase. To understand this chemical ordering transition, we have calculated the local atomic pressure represented in the Fig.5. The stress is better redistributed on each type of element (silver or platinum atoms) in the structures with concentric shells: either the full multishells structure or the partial concentric shells near the surface (multishells/$L1_1$). In the perfect $L1_1$ structure with an Ag surface shell, the majority of the stress in compression with high values (around 10 GPa) is supported by silver atoms in the core. In overall, the two structures with concentric shells are less constraints than the perfect $L1_1$ phase with an Ag shell at the surface.

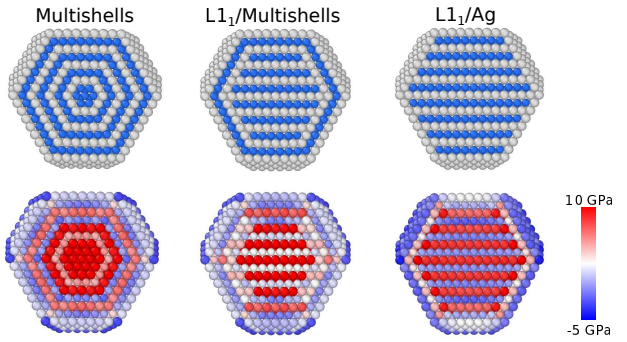

Fig. 5 Cutting view of the 2951 atoms TOh with in top row the nature of the atoms (Ag in grey, Pt in blue) and in bottom row the stress map with color code corresponding to sites in compression in red (up to 10 GPa) and sites in tension in blue (up to -5 GPa).

4 Conclusion

To conclude we have shown that in Pt-Ag nanoalloys there can be an alternative chemical ordered phase compared to the $L1_1$ phase observed experimentally[24] which consists in an alternation of pure atomic planes in the (111) direction (as expected from the bulk phase diagram). We have shown that beyond the silver surface segregation, there is also a platinum subsurface segregation coupled to a silver subshell forming a 3-concentric shells around the $L1_1$ ordered phase in the core on a quite large range of composition (between 40% and 70% of silver). What is really surprising is the apparition, in a narrow range of concentration (between 54% and 60% of Ag), of a full concentric shell structure over the whole nanoparticle, which is more stable than the $L1_1$ phase. We have shown that the concentric shells allow to release the stress in the nanoparticle as compared to the perfect $L1_1$ phase with a silver shell. Such very peculiar chemical ordering, never reported before, is established for two different sizes: 3 and 5 nm. We think it may be general when increasing the size because of the necessity to release the stress that increases with the size. We have also shown a (2x1) reconstruction on the (100) facets stable on a large range of silver concentration (from very low to equiconcetration) which can have some interesting properties in catalysis. Finally our predictions could motivate new experimental studies on Pt-Ag nanoalloys on a wider range of composition and should have strong implications in catalysis and optical properties.

Author Contributions

All authors contributed equally.

Conflicts of interest

There are no conflicts to declare.

Acknowledgements

The authors thank Riccardo Ferrando for fruitful discussion, and acknowledge support from the International Research Network-IRN "Nanoalloys" of CNRS. This work was granted access to the HPC ressources of IDRIS under the allocation 2017-096829 mage by GENCI.

Notes and references

1 *Nanoalloys: From Theory to Application*, ed. R. Johnston and R. Ferrando, RSC Publishing, 2008, vol. 138.
2 R. Ferrando, J. Jellinek and R. Johnston, *Chem. Rev.*, 2008, **108**, 845–910.
3 *Nanoalloys, Synthesis, Structure and Properties*, ed. D. Alloyeau, C. Mottet and C. Ricolleau, Springer-Verlag, London, 2012.
4 R. Ferrando, *Structure and Properties of Nanoalloys*, Elsevier, London, 2016, vol. 10.
5 M. Debe, *Nature*, 2012, **486**, 43–51.
6 Y. Pan, I. Yan, Y. Shao, J.-M. Zuo and H. Yang, *Nano Letters*, 2016, **16**, 6599–6603.
7 Z. Peng, H. You and H. Yang, *Advanced Functional Materials*, 2010, **20**, 3734–3741.
8 J. Wisniewska, I. Dziedzic and M. Ziolek, *RSC Adv.*, 2020, **10**, 14570–14580.
9 H. Liu, F. Ye, Q. Yao, H. Cao, J. Xie, J. Y. Lee and J. Yang, *Sci. Rep.*, 2014, **4**, 3969.
10 J. Cao, M. Guo, J. Wu, J. Xu, W. Wang and Z. Chen, *J. Power Sources*, 2015, **277**, 155–160.
11 X. Yang, L. T. Roling, M. Vara, A. O. Elnabawy, M. Zhao, Z. D. Hood, S. Bao, M. Mavrikakis and Y. Xia, *Nano Letters*, 2016, **16**, 6644–6649.
12 Y.-T. Pan, L. Yan, Y.-T. Shao, J.-M. Zuo and H. Yang, *Nano Letters*, 2016, **16**, 7988–7992.
13 N. M. Wilson, Y.-T. Pan, Y.-T. Shao, J.-M. Zuo, H. Yang and D. W. Flaherty, *ACS Catalysis*, 2018, **8**, 2880–2889.
14 A. Esfandiari, M. Kazemeini and D. Bastani, *Int. J. Hydrog. Energy*, 2016, **41**, 20720–20730.
15 J. Wisniewska, H. Guesmi, M. Ziolek and F. Tielens, *Journal of Alloys and Compounds*, 2018, **770**, 934–941.
16 J. Chen, B. Wiley, J. McLellan, Y. Xiong, Z.-Y. Li and Y. Xia, *Nano Letters*, 2005, **5**, 2058–2062.
17 D. Bochicchio and R. Ferrando, *Nano Letters*, 2010, **10**, 4211–4216.
18 P. Durussel and P.Feschotte, *Journal of Alloys and Compounds*, 1996, **239**, 226.
19 M. Sluiter, C. Colinet and A. Pasturel, *Phys. Rev. B*, 2006, **73**, 174204.
20 G. Hart, L. Nelson, R. Vanfleet, B. Campbell, M. Sluiter, J. Neethling, E. Olivier, S. Allies, C. Lang, B. Meredig

and C. Wolverton, *Acta Materialia*, 2017, **124**, 325.
21 C. Leroux, A. Loiseau, A. Broddin and G. V. Tendeloo, *Phil. Mag. B*, 1991, **64**, 57.
22 F. Ducastelle, *Order and Phase Stability in Alloys*, North-Holland, Elsevier Science Publishers B.V., Amsterdam, Oxford, New York, Tokyo, 1991.
23 H. Lang, T. Mohri and W. Pfeiler, *Intermetallics*, 1999, **7**, 1373–1381.
24 J. Pirart, A. Front, D. Rapetti, C. Andreazza-Vignolle, P. Andreazza, C. Mottet and R. Ferrando, *Nature Communications*, 2019, **10**, 1982–1989.
25 A. Front and C. Mottet, *Journal of Physics: Condensed Matter*, 2021, **33**, 154006.
26 A. Front, D. Oucheriah, C. Mottet and H. Amara, *Faraday Discussions*, 2023, **242**, 144–159.
27 S. Olobardi, L. Vega, A. Fortunelli, M. Stener, F. Viñes and K. M. Neyman, *The Journal of Physical Chemistry C*, 2019, **123**, 25482–25491.
28 N. Danielis, L. Vega, G. Fronzoni, M. Stener, A. Bruix and K. M. Neyman, *The Journal of Physical Chemistry C*, 2021, **125**, 17372–17384.
29 V. Rosato, M. Guillopé and B. Legrand, *Phil. Mag. A*, 1989, **59**, 321–336.
30 R. Hultgren, P. D. Desai, D. T. Hawkins, M. Gleiser and K. K. Kelley, *Selected Values of the Thermodynamic Properties of Binary Alloys*, American Society for Metals, Berkeley, Jossey-Bass Publishers, 1981, p. 777.
31 N. Metropolis, A. Metropolis, M. Rosenbluth, A. Teller and E. Teller, *J. Chem. Phys.*, 1953, **21**, 1087.
32 P. Kelires and J. Tersoff, *Phys. Rev. Lett.*, 1989, **63**, 1164–1167.
33 C. Mottet, G. Tréglia and B. Legrand, *Surface Science*, 1997, **383**, L719–L727.
34 V. Vitek and T. Egami, *Phys Status Solidi B.*, 1987, **144**, 145–156.
35 D. Nelli, C. Roncaglia and C. Minnai, *Advances in Physics: X*, 2023, **8**, 2127330.
36 A. Khoutami, B. Legrand and G. Tréglia, *Surface Science*, 1993, **287/288**, 851–856.
37 F. Tournus, K. Sato, T. Epicier, T. J. Konno and V. Dupuis, *Phys. Rev. Lett.*, 2013, **110**, 055501.